Journal of Coastal Research	SI	59	15-26	West Palm Beach, Florida	2011

An Implicit 2-D Shallow Water Flow Model on Unstructured Quadtree Rectangular Mesh

Weiming Wu[†], Alejandro Sánchez[‡], and Mingliang Zhang[†]

[†]National Center for Computational Hydroscience and Engineering
The University of Mississippi
University, MS 38677

[‡]Coastal and Hydraulics Laboratory
U.S. Army Engineer Research & Development Center,
Vicksburg, MS 39180

www.cerf-jcr.org

ABSTRACT

WU, W.; SANCHEZ, A., and ZHANG, M., 2011. An Implicit 2-D Shallow Water Flow Model on Unstructured Quadtree Rectangular Mesh. *In:* Roberts, T.M., Rosati, J.D., and Wang, P. (eds.), *Proceedings, Symposium to Honor Dr. Nicholas C. Kraus,* Journal of Coastal Research, Special Issue, No. 59, pp. 15-26. West Palm Beach (Florida), ISSN 0749-0208.

An implicit finite volume scheme is developed to solve the depth-averaged 2-D shallow water flow equations. The computational mesh consists of rectangular cells, with quadtree technology incorporated to locally refine the mesh around structures of interest or where the topography and/or flow properties change sharply. The grid nodes are numbered by means of an unstructured index system for more flexibility. The governing equations are solved using the SIMPLEC algorithm on non-staggered grid to handle the coupling of water level and velocity. In this non-staggered system, primary variables *u*-, *v*-velocity, and water level are stored on the same set of grid points, and fluxes at cell faces are determined using the Rhie and Chow's momentum interpolation method to avoid spurious checkerboard oscillations. The discretized algebraic equations are solved iteratively using the GMRES method. The model has been tested against measurement data for steady flow around a spur-dyke in a laboratory flume and tidal flows in Gironde Estuary, France and Grays Harbor, USA. The model reasonably well reproduces the temporal and spatial variations of water level and current speed observed in the measurements. The laboratory test has demonstrated that the quadtree mesh is cost-effective, while the two field cases have shown that the model is very stable and handles wetting and drying efficiently.

ADDITIONAL INDEX WORDS: *Shallow water flow equations, two-dimensional, finite volume, numerical model, quadtree rectangular mesh.*

INTRODUCTION

Because of their nonlinearity and irregular domains, most of the real-life problems of surface water flows in rivers, lakes, estuaries and coastal water bodies have to be solved numerically. The numerical methods widely used include finite difference method (FDM) (Fletcher, 1991), finite element method (FEM) (Chung, 1978; Zienkiewicz and Taylor, 2000), finite volume method (FVM) (Patankar, 1980; Ferziger and Peric, 1995; Wu, 2007), *etc.* The algebraic equations resulting from the classic, structured FDM and FVM usually have banded coefficient matrices that can be handled efficiently, whereas the algebraic equations from the unstructured FEM usually have sparse coefficient matrices that require relatively tedious effort for solution. However, the classic FDM and FVM usually adopt regular meshes and encounter difficulties in conforming to the irregular domains of surface water flows, while the FEM typically uses irregular meshes that can conveniently handle such irregular domains. Therefore, it has been a trend in recent decades to develop the FDM and FVM based on structured or unstructured irregular meshes with quadrilaterals, triangles and polygons, which have the grid flexibility of the FEM and the merits of the classic FDM and FVM.

Enhancement of accuracy of numerical solution is one of the main concerns in computational simulation of free surface flows. One may simply use high-order accurate schemes to discretize the differential governing equations for this purpose, but a high-order scheme involves more computational nodes, is more complicated and requires more computational time. Numerical schemes higher than third or fourth order have been rarely used in simulation of surface water flows. Another approach to enhancing accuracy is through refinement of mesh. Numerical discretization based on a finer mesh usually has less truncation errors and thus yields more accurate solution. However, globally refining a large, complex computational mesh is often costly, and only locally refining near boundaries and high-gradient regions is sometimes needed. For local refinement, an unstructured triangular mesh is a good choice, whereas a structured rectangular mesh is inconvenient because it refines the mesh in regions which are unnecessary. A structured quadrilateral (curvilinear) grid can serve this purpose by stretching or shrinking the mesh lines, but it is less flexible for very large, complex domains than the triangular mesh. On the other hand, the rectangular or quadrilateral mesh is more convenient than the triangular mesh for establishing high-order

DOI: 10.2112/SI59-003.1 received 20 November 2009; accepted 22 June 2010.
© Coastal Education & Research Foundation 2011

(*e.g.*, second and third) schemes or for discretizing second or higher order spatial derivatives. Therefore, quadtree (telescoping) rectangular or quadrilateral mesh has been recently used for local refinement of computational mesh in computational fluid dynamics (CFD) (Muzaferija, 1994; Ferziger and Peric, 1995; Greaves, 2004; Liang *et al.,* 2008; Nabi, 2008). On the quadtree mesh, a coarse cell is split into four child cells, and as many levels of refinement as necessary can be used. The quadtree mesh can be arranged as block-structured or completely unstructured. It is flexible in mesh generation, while keeping most advantages of the rectangular or quadrilateral mesh.

For incompressible flows such as surface water flows, the governing equations are the Navier-Stokes equations, in which the velocity is linked to the pressure gradient by the momentum equations but not the continuity equation. The continuity equation is just an additional constraint on the velocity field without directly linking to the pressure. Because of such a weak linkage, the convergence and stability of a numerical solution of the Navier-Stokes equations depends largely on the coupling between the pressure and velocity fields. Storing the variables at the geometric center of the control volume in combination with linear interpolation for internodal variation usually leads to non-physical node-to-node (checkerboard) oscillations. One approach for eliminating such oscillations is to use the staggered grid, as adopted in Harlow and Welch's (1965) MAC (Marker and Cell) method, Chorin's (1968) projection method, and Patankar and Spalding's (1972) SIMPLE (Semi-Implicit Method for Pressure-Linked Equations) algorithm. The other approach is to use the momentum interpolation technique proposed by Rhie and Chow (1983) based on the non-staggered grid. For the depth-averaged 2-D simplification of the Navier-Stokes equations in the case of shallow water flows, the linkage between the flow velocity and pressure (water level) is improved in the continuity equation, but the ware-surface-gradient terms remain in the momentum equations and the issue of coupling velocity and water level still exists somehow. In recent years, the staggered grid approaches and the Rhie and Chow's (1983) momentum interpolation method on non-staggered grid have been applied to the depth-averaged simulation of surface water flows (Wenka, 1992; Lu and Zhang, 1993; Ye and McCorquodale, 1997; Minh Duc, 1998; Kim *et al.*, 2003; Wu, 2004). In addition, several attempts (*e.g.*, Le Roux *et al.*, 1998) have been made in the FEM to eliminate the non-physical oscillations.

This paper presents recent advances in the Coastal Modeling System (CMS) for nearshore circulation developed under the Coastal Inlets Research Program (CIRP) of U.S. Army Corps of Engineers (Militello *et al.*, 2004; Buttolph *et al.*, 2006). The existing CMS circulation model (called CMS-Flow) solves the 2-D shallow water equations using an explicit FVM on structured rectangular mesh. It computes the unsteady water level and current velocity fields by solving the depth-averaged 2-D shallow water flow equations on a non-uniform Cartesian grid with an explicit finite volume scheme. It can simulate tide, wind and wave driven currents. It is two-way coupled with the spectral wave transformation model called CMS-Wave, which solves the steady-state wave-action balance equation on a non-uniform Cartesian grid with a finite difference scheme and considers wind wave generation and growth, diffraction, reflection, dissipation due to bottom friction, white capping and breaking, wave-wave and wave-current interactions, wave runup, wave setup, and wave transmission through structures (Lin *et al.*, 2008). To improve the CMS-Flow model's computational efficiency, an implicit depth-averaged 2-D scheme has been designed and tested to solve the shallow water flow equations based on a quadtree rectangular mesh. This model solves the 2-D shallow water equations for arbitrary combinations of currents and waves, considering the effect of phase-averaged wave radiation stresses on the current. The governing equations are solved within the FVM with the SIMPLEC (SIMPLE Consistent; van Doormaal and Raithby, 1984) algorithm on non-staggered grid to handle the coupling of water level and velocity. Due to limit of paper length, the numerical solution methodologies used in the new CMS flow model are the main focus here, while the wave/current interaction, bottom friction, cross-shore boundary condition, sediment and salinity transport, and many other related issues will be addressed on other occasions.

GOVERNING EQUATIONS AND BOUNDARY CONDITIONS

The depth-averaged shallow water equations in the Cartesian coordinate system are written as

$$\frac{\partial h}{\partial t}+\frac{\partial(hu)}{\partial x}+\frac{\partial(hv)}{\partial y}=0 \tag{1}$$

$$\begin{aligned}&\frac{\partial(hu)}{\partial t}+\frac{\partial(huu)}{\partial x}+\frac{\partial(huv)}{\partial y}=\\&-gh\frac{\partial\eta}{\partial x}+\frac{\partial}{\partial x}\left(\nu_t h\frac{\partial u}{\partial x}\right)+\frac{\partial}{\partial y}\left(\nu_t h\frac{\partial u}{\partial y}\right)\\&+\frac{1}{\rho}\left(\tau_{Sx}+\tau_{wx}-\tau_{bx}\right)+f_c hv\end{aligned} \tag{2}$$

$$\begin{aligned}&\frac{\partial(hv)}{\partial t}+\frac{\partial(huv)}{\partial x}+\frac{\partial(hvv)}{\partial y}=\\&-gh\frac{\partial\eta}{\partial y}+\frac{\partial}{\partial x}\left(\nu_t h\frac{\partial v}{\partial x}\right)+\frac{\partial}{\partial y}\left(\nu_t h\frac{\partial v}{\partial y}\right)\\&+\frac{1}{\rho}\left(\tau_{Sy}+\tau_{wy}-\tau_{by}\right)-f_c hu\end{aligned} \tag{3}$$

where t is the time; x and y are the horizontal Cartesian coordinates; h is the total flow depth; u and v are the depth-averaged flow velocities in x- and y-directions; η is the water surface elevation above the reference sea level; g is the gravitational acceleration; ρ is the density of flow; ν_t is the eddy viscosity due to turbulence; τ_{bx} and τ_{by} are the bed shear stresses in x- and y-directions that are determined by $\tau_{bx}=\rho c_f u\sqrt{u^2+v^2}$ and $\tau_{by}=\rho c_f v\sqrt{u^2+v^2}$; $c_f=gn^2/h^{1/3}$, in which n is the Manning's roughness coefficient; τ_{Sx} and τ_{Sy} are the wave radiation stresses in x- and y-directions; τ_{wx} and τ_{wy} are the wind

driving forces; and f_c is the Coriolis force coefficient. Because the present paper focuses mainly on the numerical solution methods of the established flow model, determination of the wind driving force and the wave radiation stresses refers to Buttolph *et al.* (2006) and Lin *et al.* (2008).

Several turbulence models, including the depth-averaged parabolic eddy viscosity model and the modified mixing length model, have been implemented in the developed model to determine the eddy viscosity ν_t. In the depth-averaged parabolic model, the eddy viscosity is calculated by $\nu_t=\alpha u_* h$, in which u_* is the bed shear velocity, $u_*=[c_f(u^2+v^2)]^{1/2}$, and α is an empirical coefficient between 0.3–1.0. It is noted that if α is set to $0.578c_f$, then the depth-averaged parabolic model reduces to the Falconer (1980) equation for eddy viscosity previously used in the CMS-Flow model.

The depth-averaged parabolic eddy viscosity model is applicable in the region of main flow but does not account for the influence of the horizontal gradient of velocity. Improvement can be achieved through combination of the depth-averaged parabolic eddy viscosity model and the mixing-length model (Wu, 2007):

$$\nu_t = \left[\left(\alpha_0 u_* h\right)^2 + \left(l_h^2 \left|\bar{S}\right|\right)^2 \right]^{1/2} \tag{4}$$

where $\left|\bar{S}\right| = \left[2\left(\partial u/\partial x\right)^2 + 2\left(\partial v/\partial y\right)^2 + \left(\partial u/\partial y + \partial v/\partial x\right)^2\right]^{1/2}$; α_0 is an empirical coefficient, set as $\kappa/6$, with κ being the von Karman constant; l_h is the horizontal mixing length, determined by $l_h = \kappa \min(c_m h, y)$, with y being the distance to the nearest wall and c_m an empirical coefficient between 0.3–1.2. The coefficient c_m is often given larger values in field cases and smaller values in laboratory cases. α_0 is smaller than α, because Equation (4) takes into account the effect of horizontal velocity gradients through the second term on its right-hand side.

For a well-defined problem governed by Equations (1)-(3), the flow discharge or velocity is needed at inflow boundaries, while the water level is usually given at outflow boundaries for a subcritical flow or at inflow boundaries for a supercritical flow. Near rigid wall boundaries, such as beaches and islands, the wall-function approach is employed. By applying the log-law of velocity, the resultant wall shear stress, $\vec{\tau}_w$, is related to the flow velocity, $\vec{V}_P$, at the center, P, of the control volume close to the wall by the following relation:

$$\vec{\tau}_w = -\lambda \vec{V}_P \tag{5}$$

where λ is a coefficient determined as $\lambda = \rho u_* \kappa / \ln\left(E y_P^+\right)$ with $y_P^+ = \rho u_* y_p / \mu$, in which μ is the dynamic viscosity, y_p is the distance from cell center P to the wall, and E is a coefficient related to wall roughness (Wu, 2007). Since λ is related to u_*, iteration is needed to solve Equation (5).

QUADTREE GRID AND DATA STRUCTURE

Because of the complexity of computational domain near coastal inlets, a simple structured rectangular mesh requires a large number of cells to resolve the detailed flow pattern near inlets, navigation channels and in-stream structures. To optimize the use of computational resources, we use the multiple-level quadtree rectangular mesh with local refinement. In this mesh, various levels of fine cells are placed close to the navigation channels and in-stream structures where the flow gradients are high, while coarse grids are used in the low-gradient regions. For simplifying the mesh, a cell is refined by splitting into four equal child cells. Corresponding to this refining, any cell has one or two faces on each of its south, north, west, and east sides. For further simplification, we eliminate those isolated single refined or coarse cells. This means that a cell should be refined if all of its adjacent cells on either x or y direction are refined, and on the other hand, a cell should not be refined if all of its adjacent cells are not refined. Through this handling, each cell has only four to six faces even though its each side may have one or two faces, as shown in Figures 1 and 2, so that the computational mesh will be less complicated.

The data structure for the quadtree mesh can be managed in several ways: block-structured, hierarchical tree, and fully unstructured. The block-structured approach divides the domain into multiple blocks, each of which is treated as structured. Interfaces between blocks are specially handled to ensure mass and momentum balance through them. The tree data structure uses parent and child relations and requires tree traverse to determine the mesh connectivity. In the fully unstructured approach, all cells are numbered in a one-dimensional sequence, and pointers are used to determine the connectivity of neighboring cells for each cell. Among the three approaches, the fully unstructured approach is simpler and thus is used in this study.

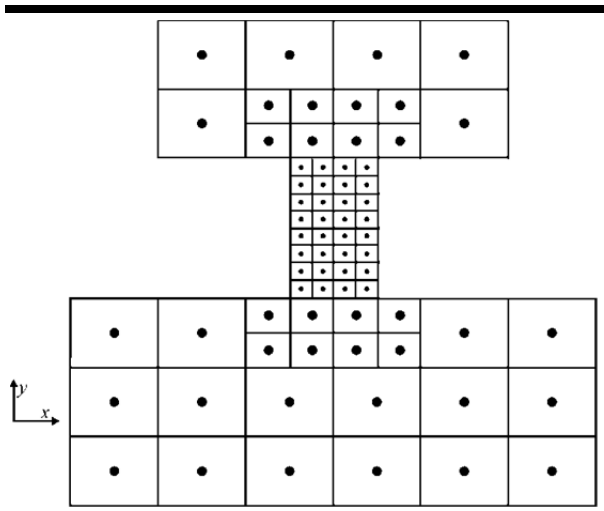

Figure 1. Example of quadtree mesh system.

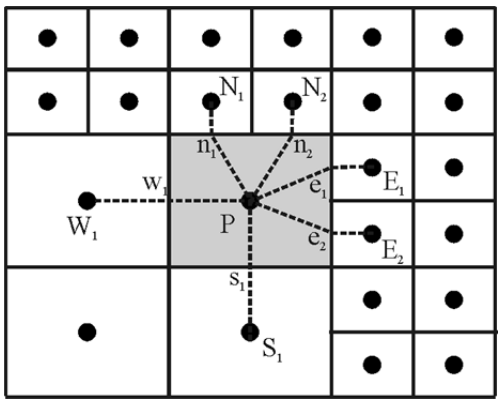

Figure 2. Control volume in a quadtree mesh.

As mentioned in the Introduction, another issue in simulation of incompressible flow is the location of primary variables: velocity and pressure (water level), related to elimination of the non-physical node-to-node (checkerboard) oscillations. One can use either staggered or non-staggered grid. On a staggered grid, the pressure is located at the center of cells and the *u*- and *v*-velocities are on the faces of cells (Harlow and Welsh, 1965; Patankar, 1980). On the non-staggered grid, all the primary variables are located at the center of cells. The staggered grid can more conveniently eliminate the checkerboard oscillations than the non-staggered grid, but the non-staggered grid results in a simpler computer code and can minimize the number of coefficients that must be computed and stored because many of the terms in each of the equations are essentially identical. In particular, the staggered grid is more complicated in handling the interface between coarse and fine cells where five- or six-face control volumes are used. Therefore, the non-staggered grid approach is adopted here, with the Rhie and Chow's momentum interpolation technique used to eliminate the checkerboard oscillations.

NUMERICAL DISCRETIZATION

Integrating the continuity equation (1) over the control volume shown in Figure 2, applying Green's theorem and discretizing the temporal derivative by the backward difference scheme, one can derive the following equation:

$$\frac{h^{n+1}-h^n}{\Delta t}\Delta A_P+\sum_{k=1}^{m_e}(hu)_{ek}^{n+1}\Delta y_{ek}-\sum_{k=1}^{m_w}(hu)_{wk}^{n+1}\Delta y_{wk}+\sum_{k=1}^{m_n}(hv)_{nk}^{n+1}\Delta x_{nk}-\sum_{k=1}^{m_s}(hv)_{sk}^{n+1}\Delta x_{sk}=0 \tag{6}$$

where Δt is the time step length; ΔA_P is the area of the control volume (cell) at node P; Δx and Δy are the lengths of the cell faces in either x or y direction; the subscripts w, e, s and n denote the west (negative x), east (positive x), south (negative y) and north (positive y) sides of the control volume; the subscript k is the index of the faces at each side, with a value of 1 or 2; and m_w, m_e, m_s and m_n are the numbers of cell faces at west, east, south and north sides of the cell. For the control volume shown in Figure 2, m_w=1, m_e=2, m_s=1 and m_n=2. For simplicity, m_w, m_e, m_s, m_n, and the superscript n+1 will be omitted in the following notations.

Defining the fluxes at cell faces as $F_{ek}=(hu)_{ek}\Delta y_{ek}$, $F_{wk}=(hu)_{wk}\Delta y_{wk}$, $F_{nk}=(hv)_{nk}\Delta x_{nk}$ and $F_{sk}=(hv)_{sk}\Delta x_{sk}$, one can rewrite Equation (6) as

$$\frac{h^{n+1}-h^n}{\Delta t}\Delta A_P+\sum_k F_{ek}-\sum_k F_{wk}+\sum_k F_{nk}-\sum_k F_{sk}=0 \tag{7}$$

Integration of the x-momentum equation over the control volume shown in Figure 2 leads to

$$\begin{aligned}&\frac{(hu)_P^{n+1}-(hu)_P^n}{\Delta t}\Delta A_P+\sum_k(huu)_{ek}\Delta y_{ek}-\sum_k(huu)_{wk}\Delta y_{wk}\\&+\sum_k(huv)_{nk}\Delta x_{nk}-\sum_k(huv)_{sk}\Delta x_{sk}\\&=-gh_P\left[\sum_k\eta_{ek}\Delta y_{ek}-\sum_k\eta_{wk}\Delta y_{wk}\right]\\&+\sum_k\left(\nu_t h\frac{\partial u}{\partial x}\right)_{ek}\Delta y_{ek}-\sum_k\left(\nu_t h\frac{\partial u}{\partial x}\right)_{wk}\Delta y_{wk}\\&+\sum_k\left(\nu_t h\frac{\partial u}{\partial y}\right)_{nk}\Delta x_{nk}-\sum_k\left(\nu_t h\frac{\partial u}{\partial y}\right)_{sk}\Delta x_{sk}+S_u\Delta A_P\end{aligned} \tag{8}$$

where S_u includes all the remaining terms. The convection terms can be discretized using several numerical schemes with upwinding capability, such as the hybrid upwind/central scheme (Spalding, 1972), exponential scheme (Spalding, 1972) and HLPA scheme (Zhu, 1991), while the diffusion terms are discretized using the central difference scheme. The hybrid scheme uses the first-order upwind or second-order central difference scheme depending on whether the Peclet number is larger than 2 or not. The exponential scheme uses the analytical solution of the linearized 1-D convection-diffusion equation to approximate the profile of the sought quantity between two neighboring cell centers; its accuracy is between first and second orders in general. The HLPA scheme uses a combination of linear and parabolic approximations for such profile, and it has second-order accuracy. Normally the HLPA scheme needs slightly more computational time and special treatments near a boundary and during the iteration because it uses more computational nodes. The details can be found in Wu (2007). In cases where higher accuracy is concerned, the HLPA scheme is a better option. However, for most of application cases, the exponential scheme is recommended because it uses about 10-20% less computational time than the HLPA scheme and has enough accuracy.

After the above manipulations, the x-momentum equation (8) reads

$$\frac{(hu)_P^{n+1}-(hu)_P^n}{\Delta t}\Delta A_P = \sum_k a_{Wk}u_{Wk}+\sum_k a_{Ek}u_{Ek}+\sum_k a_{Nk}u_{Nk}+\sum_k a_{Sk}u_{Sk} -a_P u_P - gh_P\left(\sum_k \eta_{ek}\Delta y_{ek}-\sum_k \eta_{wk}\Delta y_{wk}\right)+S_u\Delta A_P \tag{9}$$

where a_{Wk}, a_{Ek}, a_{Sk}, a_{Nk} and a_P are coefficients. Similarly, one can discretize the y-momentum equation as

$$\frac{(hv)_P^{n+1}-(hv)_P^n}{\Delta t}\Delta A_P = \sum_k a_{Wk}v_{Wk}+\sum_k a_{Ek}v_{Ek}+\sum_k a_{Nk}v_{Nk}+\sum_k a_{Sk}v_{Sk} -a_P v_P - gh_P\left(\sum_k \eta_{nk}\Delta x_{nk}-\sum_k \eta_{sk}\Delta x_{sk}\right)+S_v\Delta A_P \tag{10}$$

COUPLING OF VELOCITY AND WATER LEVEL

From the discretized momentum equation (9), one can derive the following equation for velocity u_P^{n+1}:

$$u_P^{n+1}=\frac{1}{a_P^u}\left(\sum_l a_l^u u_l^{n+1}+S_u\right)-\sum_k D_{ek}^1\eta_{ek}+\sum_k D_{wk}^1\eta_{wk} \tag{11}$$

where a_l^u denotes the coefficients for u-equation, $D_{ek}^1 = gh_P\Delta y_{ek}/a_P^u$ and $D_{wk}^1 = gh_P\Delta y_{wk}/a_P^u$. Note that the first summation in Equation (11) is applied with the index, l, sweeping over all the neighboring cells of cell P, and the temporal term on the left-hand side of Equation (9) is arranged in S_u and a_P^u in Equation (11) as suggested by Patankar (1980).

Equation (11) is used to compute the velocity for an assumed water level field in an iterative manner. Application of under-relaxation (Majumdar, 1988) leads to

$$u_P^*=\alpha_u\left(H_{1P}^*-\sum_k D_{ek}^1\eta_{ek}^*+\sum_k D_{wk}^1\eta_{wk}^*\right)+(1-\alpha_u)u_P^o \tag{12}$$

where η^* is the guessed water level, u_P^* is the approximate solution of u-velocity, u_P^o is the u-velocity in the previous iteration step, H_{1P}^* denotes the first term on the right-hand side of Equation (11) and α_u is the relaxation factor that is set as about 0.8 in this study.

There are several approaches to conduct the iteration and couple the flow velocity and water level, including the SIMPLE (Patankar and Spalding, 1972), SIMPLEC (van Doormaal and Raithby, 1984), and IDEAL (Sun *et al.*, 2009) algorithms. The SIMPLEC algorithm is used here since it has been tested well for shallow water flow modeling (Wu, 2007). One can derive the relation between the water level and velocity corrections from Equation (12):

$$u_P^{n+1}=u_P^*+\alpha_u\left(\sum_k \tilde{D}_{wk}^1\eta_{wk}'-\sum_k \tilde{D}_{ek}^1\eta_{ek}'\right) \tag{13}$$

where η' is the water level correction $\eta'=\eta-\eta^*$. In the SIMPLEC algorithm, $\tilde{D}_{wk}^1 = D_{wk}^1\Big/\left(1-\alpha_u\sum_l a_l^u/a_P^u\right)$ and $\tilde{D}_{ek}^1 = D_{ek}^1\Big/\left(1-\alpha_u\sum_l a_l^u/a_P^u\right)$. The relation of water level and velocity corrections for the SIMPLE algorithm is similar to Equation (13), with $\tilde{D}_{wk}^1$ and $\tilde{D}_{ek}^1$ replaced by D_{wk}^1 and D_{ek}^1.

Similarly, one can have the v-equation and the corresponding correction equation:

$$v_P^*=\alpha_v\left(H_{2P}^*-\sum_k D_{nk}^2\eta_{nk}^*+\sum_k D_{sk}^2\eta_{sk}^*\right)+(1-\alpha_v)v_P^o \tag{14}$$

$$v_P^{n+1}=v_P^*+\alpha_v\left(\sum_k \tilde{D}_{sk}^2\eta_{sk}'-\sum_k \tilde{D}_{nk}^2\eta_{nk}'\right) \tag{15}$$

where $H_{2P}^*=\left(\sum_l a_l^v v_l^*+S_v\right)\Big/a_P^v$, $\tilde{D}_{nk}^2 = D_{nk}^2\Big/\left(1-\alpha_v\sum_l a_l^v/a_P^v\right)$ and $\tilde{D}_{sk}^2 = D_{sk}^2\Big/\left(1-\alpha_v\sum_l a_l^v/a_P^v\right)$, with $D_{nk}^2 = gh_P\Delta x_{nk}/a_P^v$ and $D_{sk}^2 = gh_P\Delta x_{sk}/a_P^v$. Here, α_v is the relaxation factor for the v-equation.

It seems that the water surface elevation could be calculated from the discretized continuity equation (7), but in fact this might lead to spurious numerical oscillations for the collocated arrangement, as explained by Patankar (1980) and others. In order to avoid the checkerboard splitting for the collocated arrangement, we adopt the momentum interpolation technique proposed by Rhie and Chow (1983) to evaluate the variable values at cell faces from the quantities at cell centers. For example, the u-velocity at w-face and the v-velocity at s-face are determined as

$$\begin{aligned} u_{wk}^* &= \alpha_u\left[(1-f_{x,p})H_{1,PWk}^*+f_{x,p}H_{1,P}^*\right] \\ &+\alpha_u\left[(1-f_{x,p})/a_{PWk}^u+f_{x,p}/a_P^u\right]gh_{wk}\Delta y_{wk}\left(\eta_{Wk}^*-\eta_P^*\right) \\ &+(1-\alpha_u)\left[(1-f_{x,p})u_{Wk}^0+f_{x,p}u_P^0\right] \end{aligned} \tag{16}$$

$$\begin{aligned} v_{sk}^* &= \alpha_v\left[(1-f_{y,p})H_{2,PSk}^*+f_{y,p}H_{2,P}^*\right] \\ &+\alpha_v\left[(1-f_{y,p})/a_{PSk}^v+f_{y,p}/a_P^v\right]gh_{sk}\Delta x_{sk}\left(\eta_{Sk}^*-\eta_P^*\right) \\ &+(1-\alpha_v)\left[(1-f_{y,p})v_{Sk}^0+f_{y,p}v_P^0\right] \end{aligned} \tag{17}$$

and the corresponding velocity corrections as

$$u_{wk}^{n+1} = u_{wk}^{*} + \alpha_u \tilde{Q}_{wk}^{1}\left(\eta'_{Wk} - \eta'_P\right) \tag{18}$$

$$v_{sk}^{n+1} = v_{sk}^{*} + \alpha_v \tilde{Q}_{sk}^{2}\left(\eta'_{Sk} - \eta'_P\right) \tag{19}$$

where

$$\tilde{Q}_{wk}^{1} = \left[(1-f_{x,p})/a_{PWk}^{u} + f_{x,p}/a_{Pk}^{u}\right] g h_{wk} \Delta y_{wk} \Big/ \left[1-\alpha_u(1-f_{x,p})\left(\sum_l a_l^u / a_P^u\right)_{Wk} - \alpha_u f_{x,p}\left(\sum_l a_l^u / a_P^u\right)_P\right]$$

and

$$\tilde{Q}_{sk}^{2} = \left[(1-f_{y,p})/a_{PSk}^{v} + f_{y,p}/a_{Pk}^{v}\right] g h_{sk} \Delta x_{sk} \Big/ \left[1-\alpha_v(1-f_{y,p})\left(\sum_l a_l^v / a_P^v\right)_{Sk} - \alpha_v f_{y,p}\left(\sum_l a_l^v / a_P^v\right)_P\right],$$

in which $f_{x,p}$ and $f_{y,p}$ are the weighting factors used to interpolate the values of a variable at cell faces *w* and *s* from the values at two adjoining cell centers *P* and *W* or *P* and *S*, respectively; a_{PW}^u and a_{PS}^v stand for a_P^u and a_P^v when applying Equations (9) and (10) on the cells centered by *W* and *S*, respectively.

With the definition of fluxes at cell faces and Equations (18) and (19), one can derive the flux corrections at *w* and *s* faces:

$$F_{wk} = F_{wk}^{*} + a_{Wk}^{\eta}\left(\eta'_{Wk} - \eta'_P\right) \tag{20}$$

$$F_{sk} = F_{sk}^{*} + a_{Sk}^{\eta}\left(\eta'_{Sk} - \eta'_P\right) \tag{21}$$

where $a_{Wk}^{\eta} = \alpha_u \tilde{Q}_{wk}^{1} h_{wk} \Delta y_{wk}$, $a_{Sk}^{\eta} = \alpha_v \tilde{Q}_{sk}^{2} h_{sk} \Delta y_{sk}$ and F_w^* and F_s^* are the fluxes at faces *w* and *s* in terms of the velocities u_w^* and v_s^* evaluated using the Rhie and Chow's momentum interpolation method.

Inserting Equations (20) and (21) into (7) leads to the following equation for water level correction:

$$a_P^{\eta}\eta'_P = \sum_k a_{Ek}^{\eta}\eta'_{Ek} + \sum_k a_{Wk}^{\eta}\eta'_{Wk} + \sum_k a_{Nk}^{\eta}\eta'_{Nk} + \sum_k a_{Sk}^{\eta}\eta'_{Sk} + S_\eta \tag{22}$$

where $a_P^{\eta} = \sum_l a_l^{\eta} + \Delta A_P / \Delta t$, and

$$S_\eta = -\left(\eta_P^* - \eta_P^n\right)\Delta A_P / \Delta t - \left(\sum_k F_{ek}^* - \sum_k F_{wk}^* + \sum_k F_{nk}^* - \sum_k F_{sk}^*\right).$$

SOLUTION OF DISCRETIZED EQUATIONS

Because the dicretized equations are non-linear, they need to be solved iteratively. The iteration process consists of inner and outer iteration loops. The inner iteration is designed for solving each of the discretized momentum equations (12) and (14) and the water-level-correction equation (22) with an iteration solver as discussed in the next paragraphs. The outer iteration loop visits the *u*, *v* and η' equations in the following sequence in each time step as required by the SIMPLEC algorithm:

(1) Guess the water level field η^*;
(2) Solve the momentum equations (12) and (14) to obtain u_P^* and v_P^*;
(3) Use the Rhie and Chow's momentum interpolation to determine the velocities and fluxes at cell faces;
(4) Calculate η' using Equation (22);
(5) Correct η by $\eta = \eta^* + \eta'$, and update u_P and v_P using Equations (13) and (15) and fluxes using Equations (20) and (21);
(6) Treat the corrected water level, η, as a new guess, η^*, and repeat the procedure from steps 2 to 6 until a converged solution is obtained.

Because the cells on the quadtree mesh are numbered in an unstructured form, the coefficient matrices in the discretized momentum equations and the water-level-correction equation are sparse. Selection of iterative solution solvers for these algebraic equations is the key issue concerning the overall performance of the model. After a lot of testing, we have chosen a variant of the GMRES (generalized minimum residual) method (Saad, 1993) to solve the algebraic equations. The original GMRES method (Saad and Schultz, 1986) uses the Arnoldi process to reduce the coefficient matrix to the Hessenburg form and minimizes at every step the norm of the residual vector over a Krylov subspace. The variant of the GMRES method recommended by Saad (1993) allows changes in the preconditioning at every iteration step. We use the ILUT (Incomplete LU Factorization; Saad, 1994) as the preconditioner to speed up the convergence. The details of this iteration solver can be found in the above references.

Because the solution of each of the variables *u*, *v* and η' needs the updated intermediate values of other variables, it is not necessary to reach a convergent solution in each inner iteration. However, an approximately convergent solution for the η' equation (22) will ensure mass conservation at each iteration step. It is a good practice to set more iteration steps when solving Equation (22). The optimal inner and outer iteration step numbers are related to the iterative solution method, mesh size and nature of the problem. For most cases with mesh of less than 100,000 cells, if the GMRES method is used, 5, 5 and 10 inner iteration steps have been found to be good choice for Equations (12), (14) and (22), respectively, and 20 outer iteration steps are usually enough.

WETTING AND DRYING TECHNIQUES

In the numerical simulation of surface water flows with sloped beaches, barriers, spits and islands, the water edges change with time, with part of the nodes being possibly wet or dry. In the present model, a threshold flow depth (a small value

such as 0.02 m in field cases) is used to judge drying and wetting. If the flow depth on a node is larger than the threshold value, this node is considered to be wet, and if the flow depth is lower than the threshold value, this node is dry. Because a fully implicit solver is used in the present model, all the wet and dry nodes participate in the solution. Dry nodes are assigned a zero velocity. On the water edges between the dry and wet nodes, the wall-function approach is applied.

MODEL TESTING

The developed model has been recently enhanced to take into account the wave/current interactions and to simulate sediment transport and morphology changes. It has been tested extensively in many laboratory and field cases. Because the main focus of this paper is the flow solver, only three test cases are presented here. The first case is a steady flow around a spur-dyke in a laboratory flume. This case is designed to verify the developed numerical algorithms based on quadtree meshes. The second and third cases are the tidal flows in estuaries, through which the stability, efficiency and reliability of the model for unsteady flows are quantitatively validated.

Case 1: Steady Flow around a Spur-Dyke

The developed model has been tested using the measured data of Rajaratnam and Nwachukwu (1983) for the steady flow around a spur-dyke in a straight tilting rectangular flume. The flume was 37 m long and 0.92 m wide. The experimental run A1 is simulated here, in which the flume bed and walls were smooth, the spur-dyke was a thin aluminum plate of 0.152 m in length, the flow discharge was 0.0453 m^3/s, and the approach flow depth was 0.189 m.

To check whether the model results depend on the computational mesh, simulations are carried out using two quadtree meshes and a uniform mesh. The two quadtree meshes around the spur-dyke are shown in Figure 3, and both consist of three-level refinements near the spur-dyke. The finest grids cover the entire recirculation zone in quadtree mesh A, but only the region near the spur-dyke in quadtree mesh B. The finest grid spacing near the spur-dyke in both quadtree meshes is about 0.01 m in x and y directions. For comparison, a uniform mesh with this fine resolution covering the entire computational domain is also tested. The number of cells in the uniform mesh, quadtree mesh A and B is 57120, 19335, and 6482, respectively. All model parameters are set the same for the three simulation runs. The modified mixing-length turbulence model is used here, with the coefficient c_m calibrated as 0.3. The Manning's n is set as 0.012.

Figure 4 shows the flow patterns calculated using the developed model with the three meshes. For better view, certain points are skipped on the plots. One can see that the recirculation and main flow patterns simulated using the three meshes are quite similar. The recirculation zone simulated using quadtree mesh B is slightly shorter than those using the uniform mesh and quadtree mesh A. Figure 5 compares the measured and calculated depth-averaged flow velocities in cross-sections located at x/b=2, 4, 6 and 8. Here, b is the length of the spur-dyke. The model reasonably predicts the main and recirculation flows around the spur-dyke. The velocity profiles along these cross-sections among the three simulations have only very little difference. This indicates that the quadtree mesh technology is cost-effective. It has been observed that the sharp velocity gradients at the edge between the main and recirculation flow zones are under-predicted in all three runs. This is due to the zero-order turbulence model used. In order to capture such velocity gradients, a higher-order turbulence closure such as the k-ε turbulence model is preferred (Wu *et al.*, 2004).

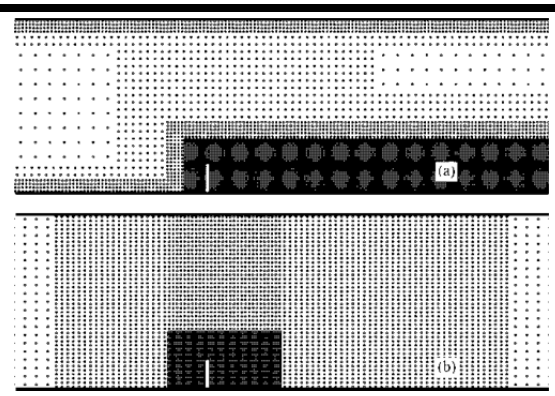

Figure 3. Meshes near a spur-dyke in a straight flume: (a) Quadtree mesh A and (b) Quadtree mesh B (Circles: locations of cell centers).

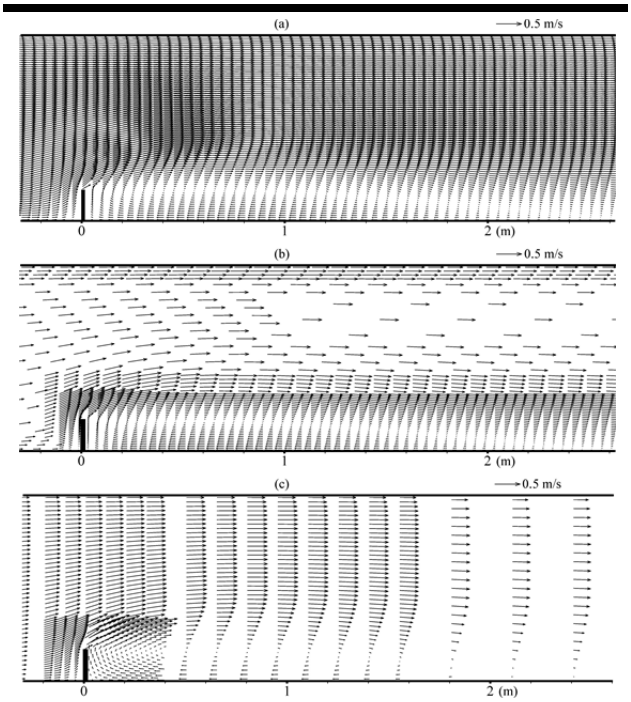

Figure 4. Calculated flow patterns near the spur-dyke using (a) Uniform mesh, (b) Quadtree mesh A, and (c) Quadtree mesh B.

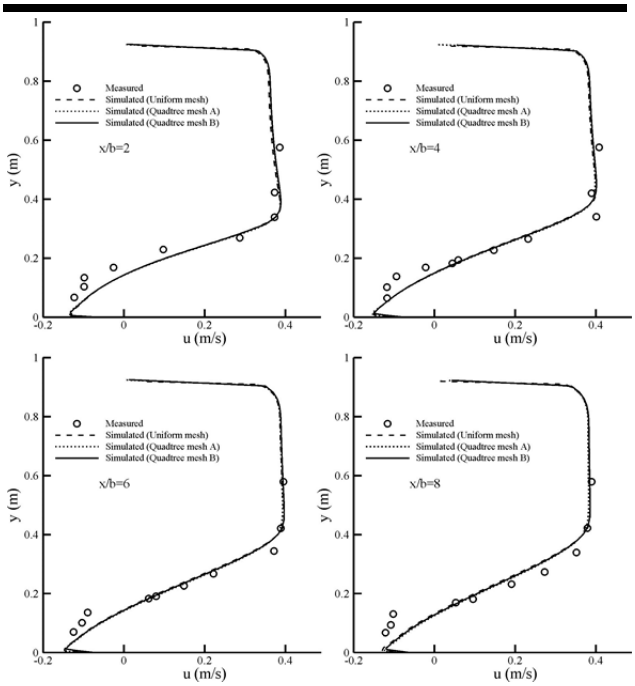

Figure 5. Comparison of measured and simulated flow velocities at selected cross-sections.

Figures 6 and 7 show the contours of velocity magnitude and water surface elevation simulated using quadtree mesh B. The recirculation flows cover several levels of refined mesh, and the transition between flows on fine and coarse grids is very smooth. This demonstrates that the numerical discretization and solution methods in the developed model are adequate to handle the unstructured quadtree mesh.

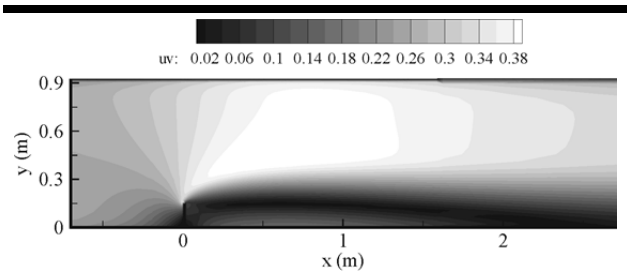

Figure 6. Calculated velocity contours.

Case 2: Tidal Flow in Gironde Estuary

The Gironde Estuary is located in southwestern France. It receives runoff from the Garonne River and the Dordogne River and empties into the Atlantic Ocean (Figure 8). The water-surface width varies from 2 to 14 km, and the flow depth in the navigation channels is about 6 – 30 m. The estuary is partially

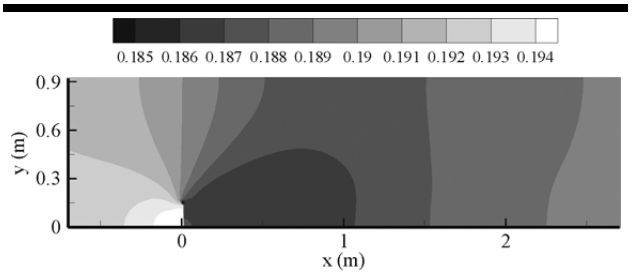

Figure 7. Calculated water level contours.

mixed and macrotidal, with a 12 hour and 25 minutes tidal lunar period and a tidal amplitude of 1.5–5 m at the mouth (Li *et al.*, 1994). The simulation domain is about 80 km long, starting from the mouth to the Garonne River and the Dordogne River.

The bed topography was provided on a uniform mesh, with a size of 250 m × 125 m for each cell. Considering the domain is relatively simple, the uniform mesh for the topography is used here as the computational mesh. It is treated as the simplest quadtree mesh, so that the developed model can handle it straightforwardly. The data measured from May 19 to 25, 1975 is used to validate the model. The computational time step is 30 minutes. At the estuary mouth, the tidal elevation is given by the recorded time series at the station "Pointe de Grave". At the two upstream ends, the flow discharges of the Garonne River and the Dordogne River are specified according to the measured data at La Réole and Pessac. The Manning's n is set as 0.015. The modified mixing-length model is used here, with the coefficient c_m set as 1.2.

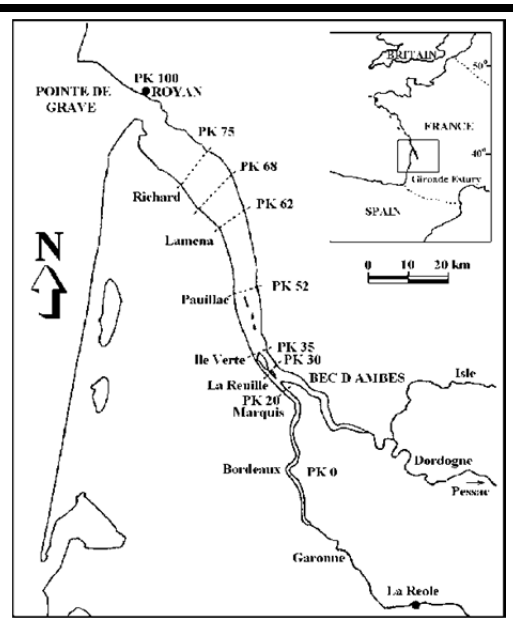

Figure 8. Sketch of Gironde Estuary, France.

The flow fields in flood and ebb tides are reasonably well predicted, as shown in Figure 9. Figure 10 compares the measured and simulated water levels at stations Ile Verte and Richard. The amplitude and phase are well predicted by the numerical model. No obvious phase difference exists between the measured and simulated tidal levels. Figure 11 shows the comparison of the measured and simulated flow velocities at stations Pauillac and Richard. The measured flow velocities are 1 m under the water surface and 1 m above the river bed, respectively. The simulated depth-averaged flow velocity stays between them. The agreement is reasonably good.

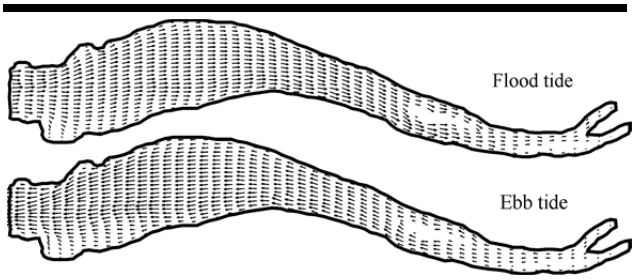

Figure 9. Simulated flow patterns in Gironde Estuary.

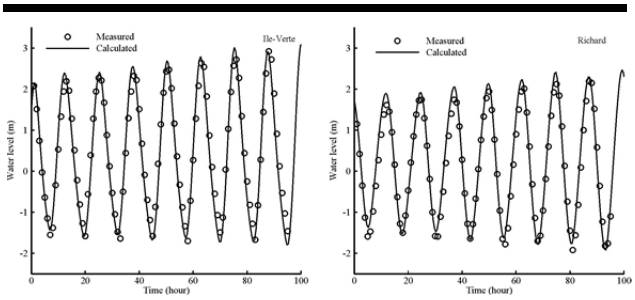

Figure 10. Measured and simulated water levels at selected stations in Gironde Estuary.

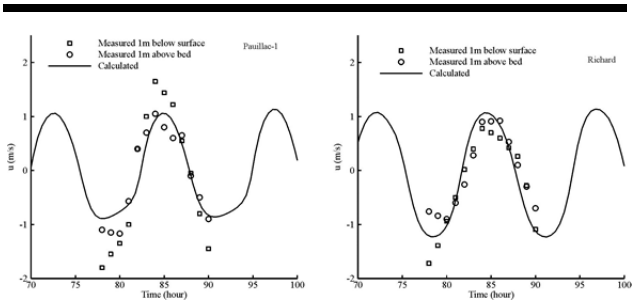

Figure 11. Measured and simulated velocities at selected stations in Gironde Estuary.

Case 3: Tidal Flow in Grays Harbor

Grays Harbor is located on the southwest Washington coast, USA, at the mouth of the Chehalis River. The estuary is one of the largest in the continental United States. As part of the U. S. Army Corps of Engineers Grays Harbor Estuary Physical Dynamics Study, current and waves were measured during September to November of 1999 (Osborne *et al.*, 2003). Figure 12 shows the plan view of the harbor and the deployed measurement stations. Figure 13 shows part of the quadtree mesh near the entrance of Grays Harbor. The mesh is refined around the jetties and near the channels, and consists of 96,100 cells. The finest grid spacing is 25 m near the jetties and the coarsest one is 800 m near the offshore boundary at deep water. The computational time step is 30 min. The measured water levels from the station nearest to the offshore boundary are used as the boundary condition. The wave radiation stresses calculated by the CMS-Wave model are considered in the simulation of current.

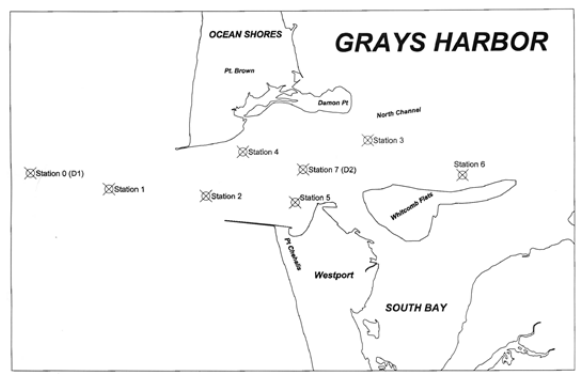

Figure 12. Measurement stations deployed in Grays Harbor in September 1999.

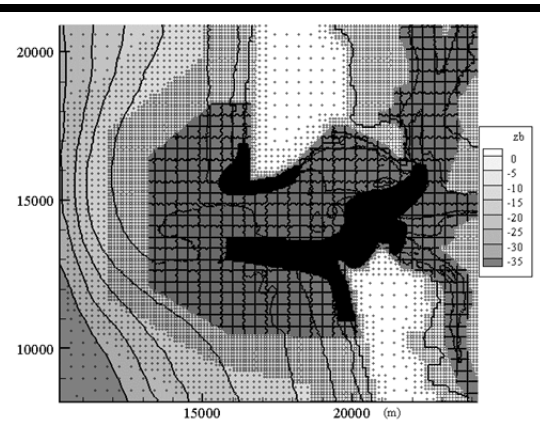

Figure 13. Computational mesh near the entrance of Grays Harbor (Dots indicate cell center locations and lines are bed elevation contours).

Figure 14 shows the simulated streamlines during ebb tide near the entrance of Grays Harbor. One can see the streamlines smoothly pass through coarse and fine mesh zones. Figure 15 shows the simulated wetting and drying processes on the floodplain in the northeast corner of the bay due to tide change. Part of the nodes are wetted during flood tide but become dry during ebb tide. This demonstrates that the model handles wetting and drying efficiently. Figure 16 compares the computed and measured water levels at Stations 4 and 5, and Figure 17 compares the computed and measured current speeds at Stations 2 and 3 for a period of six days in the late September of 1999. The model has reproduced the tidal water level and current speed reasonably well.

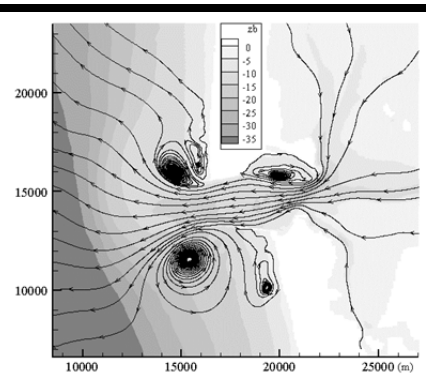

Figure 14. Simulated streamlines during ebb tide near the entrance of Grays Harbor (Background is bed elevation contours).

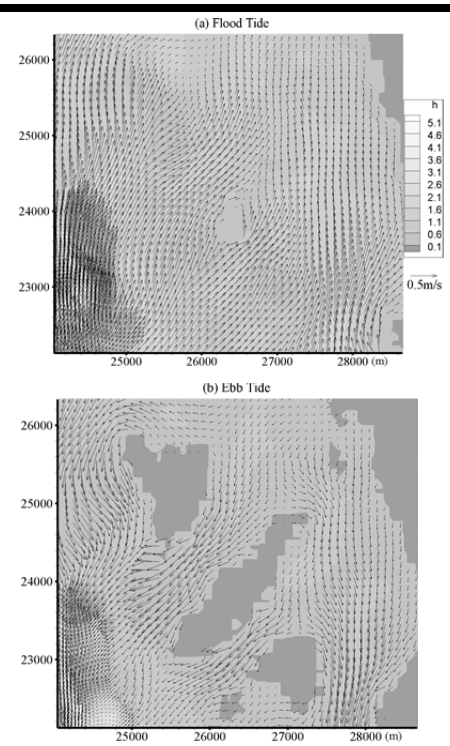

Figure 15. Floodplain wetting and drying due to tide.

CONCLUSIONS

An implicit finite volume scheme with several advanced techniques well proven in CFD has been applied to solve the depth-averaged 2-D shallow water flow equations to improve the computational efficiency of the existing CMS flow model. This new model uses an unstructured multiple-level quadtree (telescoping) rectangular mesh, which can locally refine the mesh around structures or in high-gradient regions and thus improve the accuracy of the model with a relatively small increase in number of cells. The grid points are numbered by means of an unstructured index system, so that the mesh can be flexible while it has the merits of the traditional rectangular mesh. The model uses the non-staggered (collocated) system, in which primary variables *u*-, *v*-velocity, and water level are stored on the same set of grid points, so that the interface between fine and coarse cells can be easily handled.

The convective terms in the momentum equations are discretized using one of several upwinding schemes, including the hybrid upwind/central difference, exponential difference and HLPA schemes. The HLPA scheme has second order accuracy in space, while the other two schemes have the accuracy between first and second orders. The SIMPLEC algorithm with under-relaxation is used to handle the coupling of water level and velocity and achieve high numerical stability and efficiency. Fluxes at cell faces are determined using the Rhie and Chow's momentum interpolation method, which eliminates spurious oscillations existing on non-staggered grid that can occur with linear interpolation.

Because the mesh is unstructured, the discretized algebraic equations have sparse matrices of coefficients. These equations are solved iteratively using the flexible GMRES method with ILUT preconditioning, which is efficient for solving such algebraic equations (Saad, 1993).

The first test case presented in this paper has demonstrated that the developed numerical algorithms handle quadtree meshes well and the simulated flow structures transit continuously between coarse and fine cells. The second and third test cases were used to test the developed model's robustness and reliability, showing that a time step of about a half hour can be used in simulation of tidal flow with a 12-hr period and the simulated tidal levels and velocities are in good agreement with the measured data. The model is able to handle the wetting and drying problem well and has the potential to be used in simulation of long-term processes near coastal inlets.

ACKNOWLEDGMENTS

This study is supported by the Coastal Inlets Research Program, ERDC, US Army Corps of Engineers, Vicksburg, MS. Drs. Nicholas C. Kraus, Julie D. Rosati, Lihwa Lin, Chris Reed, Alan K. Zundel, Mr. Mitchell Brown and other colleagues in the CIRP group are acknowledged for their valuable comments and suggestions.

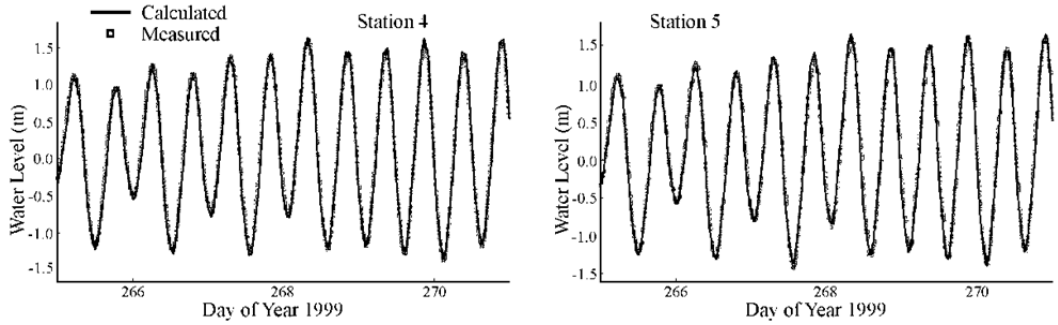

Figure 16. Measured vs. computed water surface elevations at Stations 4 and 5.

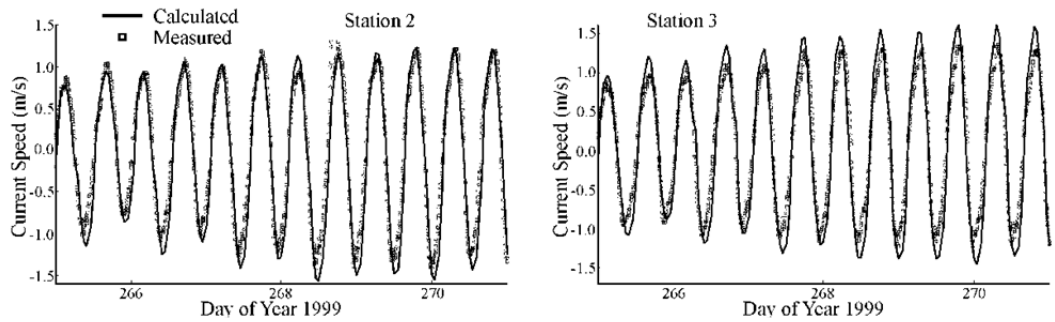

Figure 17. Measured vs. computed current speeds at Stations 2 and 3.

LITERATURE CITED

Buttolph, A. M.; Reed, C. W.; Kraus, N. C.; Ono, N.; Larson, M.; Carmenen, B.; Hanson, H.; Wamsley, T., and Zundel, A. K., 2006. Two-dimensional depth-averaged circulation model CMS-M2D: Version 3.0, Report 2: Sediment transport and morphology change. Coastal and Hydraulics Laboratory Technical Report ERDC/CHL TR-06-9. Vicksburg, MS: U.S. Army Engineer Research and Development Center, U.S.A.

Chorin, A.J., 1968. Numerical solution of the Navier-Stokes equations. *Math. Comp.*, 22, 745–762.

Chung, T.J., 1978. *Finite Element Analysis in Fluid Dynamics*. McGraw-Hill, New York.

Falconer, R. A., 1980. Modelling of planform influence on circulation in harbors. *Proceedings 17th Coastal Engineering Conference*, ASCE, 2,726–2,744.

Ferziger, J.H. and Peric, M., 1995. *Computational Methods for Fluid Dynamics*. Springer-Verlag.

Fletcher, C.A.J., 1991. *Computational Techniques for Fluid Dynamics*. Vols. 1 and 2, Springer-Verlag.

Greaves, D., 2004. A quadtree adaptive method for simulating fluid flows with moving interfaces. *J. Computational Physics*, 194(1), 35–56.

Harlow, F.H. and Welsh, J.E., 1965. Numerical calculation of time-dependent viscous incompressible flow with free surface. *Phys. Fluids*, 8, 2182-2189.

Kim, C.W.; Yoon, T.H.; Cho, Y.S. and Kim, S.T., 2003. A two-dimensional conservative finite difference model in nonorthogonal coordinate system. *J. Hydr. Res.*, IAHR, 41(4), 395–403.

Le Roux, D.Y.; Staniforth, A. and Lin, C.A., 1998. Finite elements for shallow-water equation ocean models. *Monthly Weather Review*, 126(7), 1931–1951.

Li, Z.H.; Nguyen, K.D.; Brun-Cottan, J.C. and Martin, J.M., 1994. Numerical simulation of the turbidity maximum transport in the Gironde Estuary (France). *Oceanologica Acta*, 17(5), 479–500.

Liang, Q.; Du, G.; Hall, J.W. and Borthwick, A.G.L., 2008. Flood inundation modeling with an adaptive quadtree grid shallow water equation solver. *J. Hydraulic Eng.*, ASCE, 134(11), 1603–1610.

Lin, L.; Demirbilek, Z.; Mase, H.; Zheng, J., and Yamada, F., 2008. CMS-Wave: A nearshore spectral wave processes model for coastal inlets and navigation projects. Coastal and Hydraulics Laboratory Technical Report ERDC/CHL TR-08-13. Vicksburg, MS: U.S. Army Engineer Research and Development Center, U.S.A.

Lu, Y. and Zhang, H., 1993. Numerical simulation of 2-D river-bed deformation. *J. Hydrodynamics*, Ser. A, 8(3), 273–284 (in Chinese).

Majumdar, S., 1988. Role of underrelaxation in employing momentum interpolation practice for calculation of flow with non-staggered grids. *Num. Heat Transfer*, 13, 125–132.

Militello, A.; Reed, C.W.; Zundel, A.K. and Kraus, N.C., 2004. Two-dimensional depth-averaged circulation model M2D: Version 2.0, Report 1, Technical documentation and user's guide. ERDC/CHL TR-04-2, Coastal and Hydraulics Laboratory, ERDC, US Army Corps of Engineers, Vicksburg, MS.

Minh Duc, B., 1998. Berechnung der stroemung und des sedimenttransports in fluessen mit einem tieffengemittelten numerischen verfahren. *Ph.D. Dissertation*, Karlsruhe University, Germany.

Muzaferija, S., 1994. Adaptive finite volume method for flow predictions using unstructured meshes and multigrid approach. *Ph.D. Thesis*, University of London.

Nabi, M.A., 2008. A 3D model of detailed hydrodynamics with sediment transport for simulation of subaqueous dunes. *Int. Conf. on Fluvial Hydraulics* (*River Flow* 2008), Izmir-Cesme, Turkey.

Osborne, P. D., Hericks, D. B., Kraus, N. C., and Parry, R. M. 2002. Wide-area measurements of sediment transport at a large inlet, Grays Harbor, Washington. Proc., 28th Int. Conf. on Coastal Engineering, World Scientific, Cardiff, U.K., 1–13.

Patankar, S.V. and Spalding, D.B., 1972. A calculation procedure for heat, mass and momentum transfer in three-dimensional parabolic flows. *Int. J. Heat Mass Transfer*, 15, 1787–1806.

Patankar, S.V., 1980. *Numerical Heat Transfer and Fluid Flow*. Hemisphere, New York.

Rajaratnam, N. and Nwachukwu, B.A., 1983. Flow near groin-like structures. *J. Hydraulic Eng.*, 109(3), 463-481.

Rhie, T.M. and Chow, A., 1983. Numerical study of the turbulent flow past an isolated airfoil with trailing-edge separation. *AIAA J.,* 21, 1525–1532.

Saad, Y., 1993. A flexible inner-outer preconditioned GMRES algorithm. *SIAM J. Sci. Comput.*, No. 14, 461–469.

Saad, Y., 1994. ILUT: a dual threshold incomplete ILU factorization. *Numerical Linear Algebra Appl.*, No. 1, 387-402

Saad, Y. and Schultz, M.H., 1986. GMRES: A generalized minimal residual algorithm for solving nonsymmetric linear systems. *SIAM J. Sci. Statist. Comput.*, No. 7, 856-869.

Spalding, D.B., 1972. A novel finite-difference formulation for differential expressions involving both first and second derivatives. *Int. J. Num. Meth. Engrg.*, 4, 551–559.

Sun, D.-L.; Qu, Z.-G.; He, Y.-L. and Tao, W.-Q., 2009. Performance analysis of IDEAL algorithm for three-dimensional incompressible fluid flow and heat transfer problems. Int. J. Numerical Methods in Fluids, 61(10), 1132–1160.

Van Doormal, J.P. and Raithby, G.D., 1984. Enhancements of the SIMPLE method for predicting incompressible fluid flows. *Num. Heat Transfer*, 7, 147–163.

Wenka, T., 1992. Numerische berechnung von stroemungsvorgaengen in naturnahen flusslaeufen mit einen tiefengemitelten model. *Doctoral Dissertation*, Karlsruhe University.

Wu, W., 2004. Depth-averaged 2-D numerical modeling of unsteady flow and nonuniform sediment transport in open channels. *J. Hydraulic Eng.*, ASCE, 135(10), 1013–1024.

Wu, W., 2007. *Computational River Dynamics*. Taylor & Francis, U.K., 494p.

Wu, W., Wang, P., and Chiba, N., (2004). Comparison of five depth-averaged 2-D turbulence models for river flows. *Archives of Hydro-Engineering and Environmental Mechanics*, Polish Academy of Science, 51(2), 183-200.

Ye, J. and McCorquodale, J.A., 1997. Depth-averaged hydrodynamic model in curvilinear collocated grid. *J. Hydraulic Eng.*, ASCE, 123(5), 380–388.

Zhu, J., 1991. A low diffusive and oscillation-free convection scheme. *Communication in Applied Numerical Methods*, 7, 225–232.

Zienkiewicz, O.C. and Taylor, R.L., 2000. *Finite Element Method, 5th Edition, Vol. 3: Fluid Dynamics*. Elsevier.

APPENDIX: NOTATIONS

a_{Wk}, a_{Ek}, a_{Sk}, a_{Nk}, a_P = coefficients in discretized equations
a_k^u, a_k^v, a_k^η = coefficients for u-, v- and η' equations
c_m = empirical coefficient for eddy viscosity
f_c = Coriolis force coefficient
$f_{x,p}$, $f_{y,p}$ = weighting factors for interpolation
F_{ek}, F_{wk}, F_{nk}, F_{sk} = fluxes at cell faces
g = gravitational acceleration
h = total flow depth
n = Manning's roughness coefficient
S = source term
t = time
u, v = depth-averaged flow velocities in x- and y-directions
u_* = bed shear velocity
x, y = horizontal coordinates
α_u, α_v = relaxation factors
ΔA_P = area of the control volume at node P
Δt = time step length
Δx, Δy = lengths of cell face
η = water level
η' = water level correction
ν_t = eddy viscosity
ρ = flow density
τ_{bx}, τ_{by} = bed shear stresses
subscript k = index of the faces at each side
subscript l = index of neighboring cells
subscripts w, e, s, n = west, east, south, north sides of cell
subscripts W, E, S, N = west, east, south, north adjacent nodes
superscript n = time step index
superscript o = value of previous iteration step
superscript * = guessed or approximate value